

# Perovskite Solar Cells go Outdoors: Field Testing and Temperature Effects on Energy Yield

Marko Jošt,\* Benjamin Lipovšek, Boštjan Glažar, Amran Al-Ashouri, Kristijan Brecl, Gašper Matič, Artiom Magomedov, Vytautas Getautis, Marko Topič, and Steve Albrecht

Perovskite solar cells (PSC) have shown that under laboratory conditions they can compete with established photovoltaic technologies. However, controlled laboratory measurements usually performed do not fully resemble operational conditions and field testing outdoors, with day-night cycles, changing irradiance and temperature. In this contribution, the performance of PSCs in the rooftop field test, exposed to real weather conditions is evaluated. The 1 cm<sup>2</sup> single-junction devices, with an initial average power conversion efficiency of 18.5% are tracked outdoors in maximum power point over several weeks. In parallel, irradiance and air temperature are recorded, allowing us to correlate outside factors with generated power. To get more insight into outdoor device performance, a comprehensive set of laboratory measurements under different light intensities (10% to 120% of AM1.5) and temperatures is performed. From these results, a low power temperature coefficient of  $-0.17\% \text{ K}^{-1}$  is extracted in the temperature range between 25 and 85 °C. By incorporating these temperature- and light-dependent PV parameters into the energy yield model, it is possible to correctly predict the generated energy of the devices, thus validating the energy yield model. In addition, degradation of the tested devices can be tracked precisely from the difference between measured and modelled power.

## 1. Introduction

In recent years, perovskite-based solar cells have shown extraordinary progress in reaching high power conversion efficiencies (PCE) with the current record standing at 25.2% for a perovskite single-junction device, which is substantially better than CIGS and CdTe and within reach of silicon solar cells.<sup>[1]</sup> However, in order for perovskites to successfully enter photovoltaic market, scalability and stability also need to be ensured. The latter especially has been one of the main causes of skepticism for a long time. The current  $T_{80}$  lifetime standard in the photovoltaic field, i.e., the time when PCE of the module drops down to 80% of its initial PCE, is around 30 years, while the perovskites solar cells are yet notorious for poor long-term stability. The main degradation factors arise from their compositional instability,<sup>[2]</sup> ion migration, and halide/metal reactivity,<sup>[3–5]</sup> as well as moisture, oxygen and UV light sensitivity.<sup>[6–8]</sup> In addition,

the charge selective contacts are also not immune to degradation.<sup>[9,10]</sup> As a result, a lot of research effort has been directed toward better understanding and avoidance of the separate degradation modes.


The first step toward this goal is to thoroughly observe performance of the operating solar cells, and for this, it is imperative to utilize relevant testing conditions. Several different testing procedures have been applied, with most if not all of the analysis conducted under controlled conditions in the laboratory. The most common ones are off-the-shelf stability, constant MPP tracking at 25 °C or at elevated temperatures,<sup>[11,12]</sup> or aging samples first under elevated temperature (constant or cycling) but measuring finally at 25 °C.<sup>[13–18]</sup> A few groups have investigated aging of the devices under outdoor conditions, however, instead of MPP tracking those cells were kept at open-circuit condition and  $I$ – $V$  measurements in regular intervals were performed, either outdoors<sup>[19–21]</sup> or in the laboratory.<sup>[22,23]</sup> As expected, elevated temperatures speed up the degradation process of perovskite devices.<sup>[24]</sup> Degradation is faster at open-circuit conditions due to the higher excess charge carrier concentration creating additional recombination centers, but it is also present at MPP conditions.<sup>[25]</sup> Schwenzer et al. have tested the stability of perovskites under temperature cycling; they observed a linear decrease in open-circuit

Dr. M. Jošt, A. Al-Ashouri, Prof. S. Albrecht  
Young Investigator Group Perovskite Tandem Solar Cells  
Helmholtz-Zentrum Berlin  
Kekuléstraße 5, Berlin 12489, Germany  
E-mail: marko.jost@fe.uni-lj.si

Dr. M. Jošt, Dr. B. Lipovšek, Dr. B. Glažar, Dr. K. Brecl, Dr. G. Matič,  
Prof. M. Topič  
Faculty of Electrical Engineering  
University of Ljubljana  
Tržaška 25, Ljubljana 1000, Slovenia

Dr. A. Magomedov, Prof. V. Getautis  
Department of Organic Chemistry  
Kaunas University of Technology  
Radvilenu pl. 19, Kaunas LT-50254, Lithuania

Prof. S. Albrecht  
Faculty IV-Electrical Engineering and Computer Science  
Technical University Berlin  
Marchstraße 23, Berlin 10587, Germany

 The ORCID identification number(s) for the author(s) of this article can be found under <https://doi.org/10.1002/aenm.202000454>.

© 2020 The Authors. Published by WILEY-VCH Verlag GmbH & Co. KGaA, Weinheim. This is an open access article under the terms of the Creative Commons Attribution License, which permits use, distribution and reproduction in any medium, provided the original work is properly cited.

DOI: 10.1002/aenm.202000454

voltage ( $V_{OC}$ ) of around  $-0.11\% K^{-1}$  and a severe degradation in short-circuit current ( $J_{SC}$ ), which, however, was reversible after several hours of light-soaking.<sup>[26]</sup> Nevertheless, with the improvements in material and solar cell fabrication, the devices are now even passing standardized protocols, such as IEC 61215, involving indoor tests in which modules are heated up to  $85\text{ }^{\circ}C$  for 1000 h at 85% relative humidity and temperature cycles from  $-40$  to  $90\text{ }^{\circ}C$  up to 100 times. The IEC tests for perovskite solar cells are orderly summarized in.<sup>[27]</sup> In addition, a consensus statement for reporting and assessing stability of perovskite solar cells based on ISOS procedures has recently been agreed.<sup>[28]</sup> However, while these measurements and aging procedures are a good indicator of long term stability and are valid for established technologies such as silicon, they do not fully resemble the outdoor operational conditions, with regular day-night cycles, where irradiance and air temperature simultaneously change. This is especially critical for perovskite solar cells, due to their unique characteristics compared to other conventional high efficiency solar cells, most importantly ion migration,<sup>[29]</sup> as such conditions might affect their long term stability and energy output.<sup>[30]</sup> It has been shown recently that indoor testing cannot fully suggest their outdoor stability under operational conditions.<sup>[23,31]</sup> For example, the regular polling and electric field intensity changes during day-night cycles cause regular ion redistribution,<sup>[8,32]</sup> which seems to be reversible, however, combined with temperature they might in the long-term potentially create new recombination centers in the perovskite bulk or at the interfaces.<sup>[31]</sup> Despite that, operational conditions are rarely considered. Only few reports can be found, even for day-night cycling only, all conducted in the laboratory conditions.<sup>[8,32,33]</sup> Recently, Tress et al. analyzed the typical operational performance applying real temperature and light intensity profiles but under controlled lab conditions.<sup>[34]</sup> Interestingly, all reports show that with an increasing time of testing, perovskite devices suffered some irreversible and reversible degradation, which potentially cannot be detected in a constant temperature, constant one-sun AM1.5 irradiance MPP track. It is unclear whether this might be overcome with future optimizations or is an intrinsic property of perovskite. The above further highlights the necessity for outdoor testing under real operational conditions. Such measurements would help to investigate degradation processes, focusing on the elimination of the main causes of decreased performance.

Besides outdoor conditions affecting the stability, the sun spectra and air temperature can heat up the module and thus have a strong effect on PCE and consequently energy yield of all PV devices. While standard testing conditions (STC) define the cell temperature of  $25\text{ }^{\circ}C$  during the measurements, under operational conditions solar modules can easily reach  $70\text{ }^{\circ}C$  and more for several hours. The most basic temperature effect can be calculated using a detailed balance limit (DBL):<sup>[35]</sup> e.g., by heating the cell from  $25$  to  $70\text{ }^{\circ}C$  the DBL PCE drops from 33.7% to 31.8% respectively, thus temperature has a negative effect on device performance. This change corresponds to a power temperature coefficient  $\gamma = k_{th,P} = -0.13\% K^{-1}$ , when normalized with a PCE. The effect of temperature on  $J$ - $V$  characteristics, derived from the DBL theory, is shown in Figure S1 (Supporting Information) with the calculated PCE shown as an inset. The drop in PCE is mainly due to a drop in  $V_{OC}$ , a

drop of  $\approx 50\text{ mV}$  is expected only due to increased temperature for a  $\Delta T = 45\text{ K}$ , caused by increased blackbody radiation from the warmer solar cell. The  $J_{SC}$ , on the other hand, depends only on the sun spectra and thus does not change in the DBL calculations. The detailed analysis of  $J_{SC}$ ,  $V_{OC}$ , and fill factor FF and their dependence on bandgap and temperature can be found in.<sup>[36]</sup> In addition, also material properties can have a temperature dependence, for example,  $J_{SC}$  of silicon solar cells increases under increased temperature due to the narrowing of the bandgap. Thus, knowledge of the performance under elevated temperatures is important for understanding and predicting outdoor solar cell performance.

For other technologies, temperature-dependent characteristics with well-established temperature coefficients have been reported.<sup>[37-39]</sup> For perovskites, on the other hand, only a few reports are available which overall differ significantly: in the early reports, a relatively high  $k_{th,P}$  in the range from  $-0.33$ <sup>[40]</sup> to  $-0.7\% K^{-1}$ <sup>[41,42]</sup> were obtained, most likely due to nonoptimized perovskite solar cells. In 2016, Fu et al. have measured a much lower  $k_{th,P} = -0.18\% K^{-1}$ <sup>[43]</sup> utilizing a semi-transparent p-i-n stack. Recently, Deng et al. reported a  $k_{th,P} = -0.13\% K^{-1}$  for a 15% solar cell with a blade coated perovskite absorbers,<sup>[44]</sup> which is on par with minimal values derived from thermodynamic limits in DBL theory as explained above. Sometimes reports also show a nonlinear  $k_{th,P}$ ,<sup>[34]</sup> which is attributed to the used hole-transporting material Spiro-OMeTAD. Spiro-OMeTAD has temperature-activated charge transport, and also limits the tested temperature range to  $50\text{ }^{\circ}C$  due to its low glass transition temperature, thus not suitable for high-temperature applications.<sup>[45]</sup> On the other hand, Gehlhaar et al. have studied temperature effects from the other point of view: they measured perovskite module operational temperatures under different incident irradiation densities and ambient air temperatures,<sup>[46]</sup> which helps understand and predict operational temperatures of perovskite modules. Knowing temperature characteristics and operational temperature of perovskite solar cells is necessary for energy yield predictions.

Energy yield (or energy output) is a valuable quantity of evaluating the performance of solar cells and modules under outdoor conditions, and is a very important aspect for practical applications. Such an analysis is already quite common for perovskite/silicon tandem solar cells,<sup>[47-50]</sup> but temperature dependency is usually neglected. In reports that do discuss temperature effects, the question remains whether all the effects of the temperatures were considered. H6ranthner and Snaith show temperature-dependent one-diode modeling of perovskite single-junction and perovskite/silicon tandem with preliminary results shown in the Supporting Information.<sup>[47]</sup> They theoretically derive the  $k_{th,P}$  to be  $-0.165\% K^{-1}$ , but do not calculate the energy yield due to lack of reliable data, such as device operational temperature. A more complete approach has recently been published by Schmager et al. where they presented the methodology behind energy yield calculations and assumed literature values for temperature dependency.<sup>[50]</sup> However, the complete tandem modeling is more complex due to temperature-dependent bandgap shifting, spectrally and possibly thermally induced current mismatch and consequent fill factor correction.<sup>[51,52]</sup> Thus it is important to fully understand the behavior of the subcells first, in this case, the perovskite, since their properties are less investigated. Tress et al.<sup>[34]</sup> analyzed

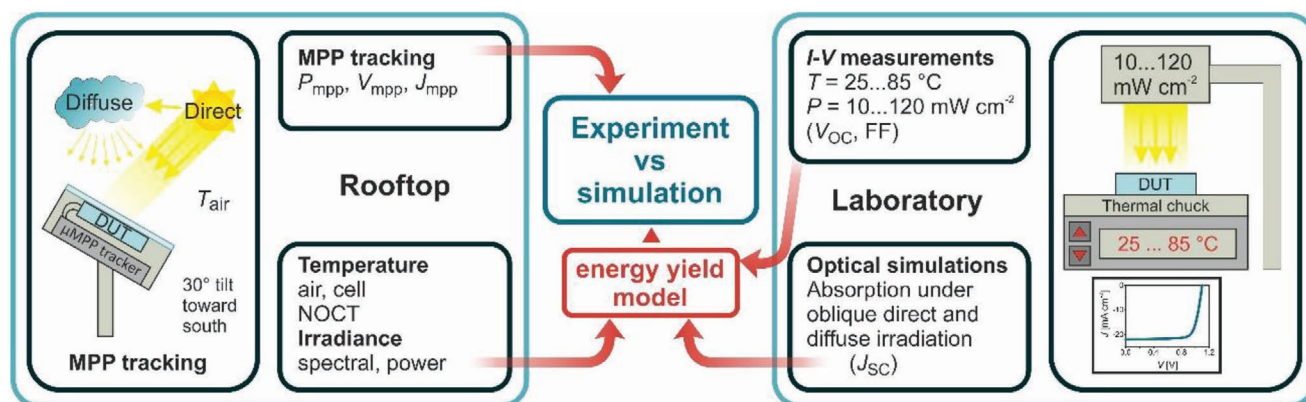


**Figure 1.** Schematic presentation of the procedures utilized. The perovskite single-junction solar cells were tracked in MPP on the rooftop. During the tracking, weather data (irradiance, temperature) were collected (left side). In parallel, similar devices were measured in the laboratory under different light intensities and elevated temperatures (right side). From the data obtained, a temperature dependent energy yield model was developed, allowing us to predict energy output or track the degradation.

the temperature effect on the energy yield, based on laboratory measurements. However, they did not include spectral changes and diffuse irradiation, which are key components of outdoor conditions.

Overall, for perovskite solar cell outdoor testing reports are scarce and temperature-dependent analysis is mostly focused on power temperature coefficients, neglecting current ( $J_{SC}$ ,  $J_{MPP}$ ), voltage ( $V_{OC}$ ,  $V_{MPP}$ ) and fill factor dependency on irradiance and temperature. Thus more data and knowledge are needed to clearly rate the stability and degradation of perovskite solar cells under operational outdoor conditions and to forecast the energy yield of perovskite-based cells and modules in the future.

In this contribution, we perform a first true MPP tracking analysis of perovskite single-junction solar cells under outdoor conditions, which are further corroborated by systematic laboratory measurements. The testing procedure is schematically presented in **Figure 1**. The fabricated  $1 \text{ cm}^2$  area devices with an average PCE of 18.5% are encapsulated and placed on the rooftop. Their power output is tracked at maximum power point (MPP) and all relevant weather data are recorded simultaneously. From this, the influence of outside conditions, such as irradiation and temperature on the performance is analyzed. In parallel, a number of similar devices are tested in controlled laboratory conditions under different light intensities from 10% to 120% of AM 1.5g and elevated temperatures (IEC 61853<sup>[53]</sup>) from 25 to 85 °C, from which the temperature coefficient and light intensity dependence are extracted. Using a full set of temperature-dependent PV performance parameters ( $J_{SC}$ ,  $V_{OC}$ , and FF), we develop a first perovskite single-junction temperature dependent energy yield model for the given high-efficiency perovskite solar cell. Not only that, we obtain an excellent match with the measurements on the rooftop, thus demonstrating the first validation of energy yield calculations for perovskite solar cells. The model enables easy real-time evaluation of the rooftop data which is otherwise challenging due to changing weather conditions. We observe that the matching between MPP tracks and our model is very good in beginning, but is increasing with time. We ascribe this to the degradation of our devices, which is confirmed by  $I$ - $V$  measurements, performed on the rooftop

with our MPP tracker. Thus, with the developed temperature dependent energy yield model, we can not only predict energy output under any climate conditions, but also to track the degradation of devices precisely.

## 2. Results

### 2.1. Device Structures

To analyze the outdoor and temperature dependence for perovskite single-junction solar cells, we utilize the p-i-n (so-called inverted) configuration. This configuration has been shown to be very robust during humidity and temperature stress tests<sup>[5,13]</sup> and is more suitable for our tests compared to n-i-p spiro-OMeTAD based devices, because of the associated degradation.<sup>[54,55]</sup> Additionally, p-i-n configuration is also utilized in state-of-the-art tandem solar cells,<sup>[48,51]</sup> thus some of our results could easily be transferred to tandem devices. The layer stack of our devices is as follows: glass|ITO|MeO-2PACz|perovskite| $\text{C}_{60}$ | $\text{SnO}_2$ |Cu. The perovskite absorber used here is a typical “triple cation”  $\text{Cs}_{0.05}(\text{FA}_{0.83}\text{MA}_{0.17})\text{Pb}_{1.1}(\text{I}_{0.83}\text{Br}_{0.17})_3$ .<sup>[56]</sup> The molecule MeO-2PACz forms a self-assembled monolayer and acts as a highly efficient hole selective contact.<sup>[57]</sup> The metal-oxide  $\text{SnO}_2$  as interfacial or barrier layer was used between  $\text{C}_{60}$  and metal electrode to improve the temperature resistance and long-term stability of the devices.<sup>[58]</sup> As will be shown below, the devices with  $\text{SnO}_2$  survived the temperature tests without degradation, confirming our choice of device architecture.

In the scope of our research, devices with two different areas were used. For laboratory experiments, we fabricated solar cells with a smaller active area of  $0.16 \text{ cm}^2$ , which is the standard lab scale testing area size. The substrates contained 6 devices each; one device was tracked, while the others were not measured but kept at  $V_{OC}$  under light-soaking conditions. For the outdoor testing, we fabricated large area ( $>1 \text{ cm}^2$ ) single-junction perovskite solar cells with one device per substrate. The larger area was used since it has a larger area-to-edge ratio and this design facilitated encapsulation and contacting; these devices were

covered with a glass slide and sealed with a two-component encapsulant (see Figure S3, Supporting Information) to ensure a longer lifetime under outdoor conditions. Despite larger area, only a negligible drop in PCE was observed; an average PCE of 18.5% at STC was achieved with both designs (Figure S2, Supporting Information).

## 2.2. Outdoor Performance

The outdoor testing was performed on the rooftop testing site at the University of Ljubljana from August to November. The encapsulated 1 cm<sup>2</sup> devices were put in a closed, sealed plastic box to further prevent penetration of moisture and oxygen to the active area of the device. The top side of the box was a glass cover. The so-prepared devices were then placed on the rooftop facing south under the tilt angle of 30°. Figure 1 shows schematically the outdoor testing setup with all the relevant details, while Figure S4 (Supporting Information) shows a photograph of the rooftop testing site. The devices were MPP-tracked using an internally developed  $\mu$ MPP tracker, which can also perform  $I$ - $V$  measurements at regular intervals. The details on  $\mu$ MPP hardware will be published elsewhere. The temperature of the cell together with the air temperature was recorded. Additionally, a spectrometer and pyranometer recorded the spectral distribution of solar irradiance over time and its integrated power, respectively.

Figure 2 shows the data of the two selected days of the rooftop testing. The data over the course of 6 days in September 2019, from which those two days were selected, are shown in Figure S5 (Supporting Information). Figure 2a displays a strong interconnection between the solar irradiance  $G_{\text{inc}}$  (shown in light blue), the temperature of the cell  $T_{\text{cell}}$  (red) and generated electrical power  $P$  (black). The solar irradiance dictates both the  $T_{\text{cell}}$  and its electrical output. All the irradiance changes are almost instantly shown (the temperature heating/cooling rate of 3.1 K min<sup>-1</sup> was predicted in<sup>[46]</sup>) and the generated electrical power reacts accordingly. The maximum achieved temperature of the cell was  $\approx 60$  °C. In Figure 2b, the electrical performance of the same solar cell is shown in more detail with parameters  $P$ ,  $V_{\text{MPP}}$  and  $J_{\text{MPP}}$  overlaid. The shape of  $P$  and  $J_{\text{MPP}}$  are almost identical, while the  $V_{\text{MPP}}$  stays relatively constant around 0.9 V

over the course of the day when the device is producing power. This is reasonable due to the logarithmic dependence of photovoltage on illumination intensity (for constant FF). Additionally, a stronger drop in  $V_{\text{MPP}}$  under higher temperature is counterbalanced by an increase due to higher solar irradiance as will be shown below. Whether this is a general case or only a specific case connected with conditions during our tests remains to be tested.

Next, we focus on the temperatures. In most laboratory experiments,  $T_{\text{cell}}$  is usually determined by the heating/cooling stage located of the solar cell sample holder. Outdoors, in the solar modules,  $T_{\text{cell}}$  is typically determined indirectly by the air temperature  $T_{\text{air}}$  and  $G_{\text{inc}}$ . Additional effects, such as device performance and module specifics like color, amount of reflection and absorption can all be summarized in the parameter NOCT, which stands for the nominal operating cell temperature and is defined as  $T_{\text{cell}}$  at 20 °C air temperature, 1 m s<sup>-1</sup> wind speed, and 800 W m<sup>-2</sup> total irradiance. Using NOCT,  $T_{\text{cell}}$  can empirically be calculated from an arbitrary combination of  $T_{\text{air}}$  and  $G_{\text{inc}}$

$$T_{\text{cell}} = \frac{\text{NOCT} - 20 \text{ }^{\circ}\text{C}}{800 \text{ W m}^{-2}} \cdot G_{\text{inc, total}} + T_{\text{air}} \quad (1)$$

For silicon modules NOCT = 44 °C is usually used, despite the values ranging somewhere between 41 and 47 °C.<sup>[59]</sup> Using these two NOCT values, 41 and 47 °C, for a silicon solar cell with PCE = 20% and  $k_{\text{th, P}} = -0.4\%$  K<sup>-1</sup>, the difference in PCE at 1000 W m<sup>-2</sup> and 25 °C air temperature (STC) would be 0.6% absolute. For perovskite devices or modules, however, there are only few reports on NOCT. In the previously mentioned report by Gehlhaar et al.,<sup>[46]</sup> the authors predict the module temperature at NOCT conditions to be around 43 °C, which fits well with silicon modules. Nevertheless, different PCE values and bandgaps, causing different thermalization and long wavelength losses could affect NOCT value.

Using Equation (1) and measured  $T_{\text{air}}$ ,  $T_{\text{cell}}$ , and  $G_{\text{inc}}$ , we are able to calculate NOCT of our tested perovskite single-junction devices. Figure 3a shows the difference between the  $T_{\text{cell}}$  and  $T_{\text{air}}$  in dependence of solar irradiation. Using a linear fit, we estimate the NOCT for our system to be 43 °C. The value is in line with the silicon modules and fits with the results reported

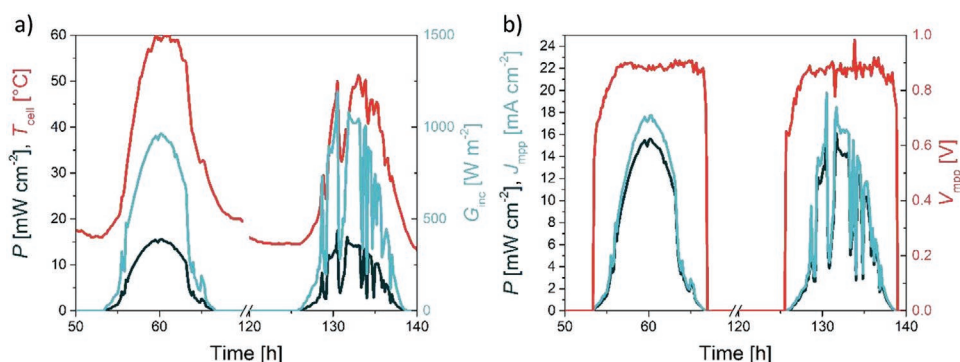


**Figure 2.** a) Solar irradiance (blue), the temperature of the tested cell (red) and the power (black) generated by the solar cell tested on the rooftop for two selected days. b) Detailed analysis of the generated power, decomposed into  $J_{\text{MPP}}$  and  $V_{\text{MPP}}$  for the same two days. The two graphs for the course of 6 consecutive days are shown in Figure S5 (Supporting Information).

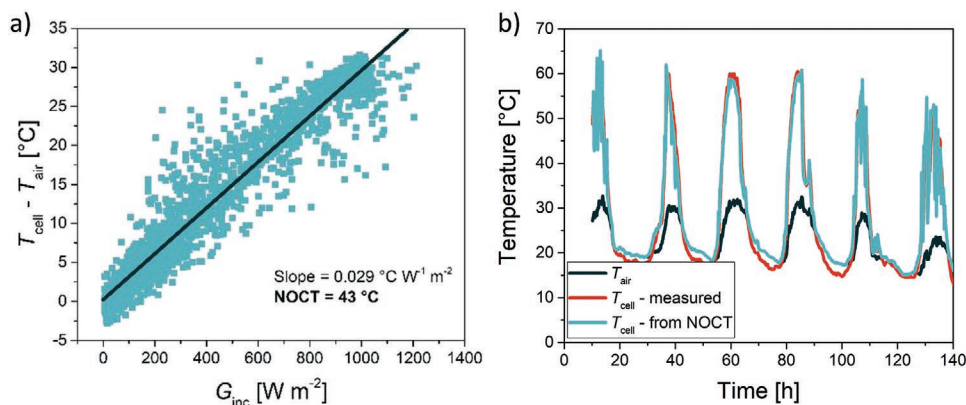


**Figure 3.** a) Dependence of irradiance on the temperature increase of the solar cell ( $T_{cell} - T_{air}$ ). From the slope (black line), parameter NOCT can be determined, in our case NOCT = 43 °C. b) Comparison between the measured  $T_{cell}$  and cell temperature calculated from  $T_{air}$  and NOCT.

by Gehlhaar et al.<sup>[46]</sup> Checking back, using our calculated NOCT parameter to predict  $T_{cell}$  from  $T_{air}$ , we get good matching with the measured cell temperature over several days during the daytime, as shown in Figure 3b. Thus, following Gehlhaar and our results, when only  $G_{inc}$  and  $T_{air}$  are available, but not also  $T_{cell}$ , a NOCT = 43 °C can reliably be used to predict  $T_{cell}$ .

While the rooftop MPP tracking provides useful data on the operation ( $P$ ,  $J_{MPP}$ ,  $V_{MPP}$ ) of solar cells, it is challenging to evaluate how the devices are actually performing due to changing irradiance and temperature, even from  $J-V$  curves that were obtained during rooftop testing (see Figure S6 in the Supporting Information for graphs and discussion). Thus we turn to controlled conditions in the laboratory and systematically investigate performance under different, well-controlled light intensities and temperatures.

### 2.3. Laboratory Conditions

These tests were conducted in air and the devices were not encapsulated. For contacting, a thermally coupled copper sample holder was used, placed on a temperature-controlled chuck. The device was in direct contact with the holder and reached the desired set temperature within a few minutes, as confirmed by the stabilized power output.

Two different laboratory tests were performed. In the first one, the solar cell is tracked under one-sun AM1.5 conditions ( $100 mW cm^{-2}$ ) in MPP. To determine the performance under elevated temperature, the temperature was simultaneously altered during the tracking in 15 °C steps between 25 and 85 °C and back to 25 °C within  $\approx 150$  min as shown in Figure 4a. Lower temperatures were not considered due to potential water condensation forming on the devices in the humid air. Before each temperature change, we waited  $\approx 15$  min for the MPP to stabilize. The initial PCE at 25 °C is 18.3% and stable over 10 min of tracking. Upon the temperature change to 40 °C, the PCE immediately drops by 0.5% absolutely, with a similar trend happening for each of the temperature increment. At 85 °C a PCE of 16.4% is measured, meaning the PCE dropped by around 1.8% absolute for a  $\Delta T = 60$  K. When lowering the temperature from 85 °C back to 25 °C, the starting PCE of 18.3% was reached again. In

general, the PCE at the same temperatures during the cooling and heating cycle are very similar (see also Figure 4b), thus we can exclude short-term degradation effects of the device under test during the measurement. This excellent operational stability even at 85 °C is attributed to our selection of stable charge transport layers (MeO-2PACz and  $SnO_2$ ). Nevertheless, the devices kept under  $V_{OC}$  during the temperature test degraded considerably (see Figure S7, Supporting Information).

The drop in PCE is mostly connected to the drop in  $V_{MPP}$ : the difference between 25 and 85 °C is around  $\approx 80$  mV, which is the same value as predicted in the DBL. At the same time, the predicted DBL  $V_{OC}$  drop is only 60 mV due to a FF drop. The  $J_{MPP}$  changes also occur, especially immediately after the temperature change. When the temperature was increased, then the initial drop is followed by a slow (a couple of minutes) increase in  $J_{MPP}$ ; when the temperature was lowered, the initial increase is followed by a slow decrease. Overall,  $J_{MPP}$  drops with temperature, approximately by  $0.4 mA cm^{-2}$  for a  $\Delta T = 60$  K.

From the data above, we can determine the temperature coefficient by extracting the  $PCE_{MPP}$  values just before the next temperature step. Plotting PCE versus temperature, we see a clear linear dependence as shown in Figure 4b, with a slope of  $-0.03\%_{abs} K^{-1}$ . The obtained slope is then normalized with the device PCE at STC (18.3%), to finally get  $k_{th,P} = -0.17\%_{rel} K^{-1}$ . This value is lower than that for silicon devices, e.g., state of the art SunPower's silicon modules with  $-0.29\% K^{-1}$ <sup>[60]</sup> or  $0.39\% K^{-1}$  for a standard monocrystalline module,<sup>[61]</sup> and fits with report by Fu et al.<sup>[43]</sup> We also added guides to the eye for the  $k_{th,P}$  in the range between 0.05% and 0.3%  $K^{-1}$  that show a clear difference between different slopes. Additionally, we have tested a few devices from different batches. They all showed very similar temperature coefficients between 0.15 and 0.2%  $K^{-1}$  as shown in Figure S8 (Supporting Information).

The above tests were made under a sun simulator at  $100 mW cm^{-2}$  illumination intensity, which in outdoor operation is rarely the case due to the ever-changing weather conditions. Therefore, in the second test, we perform light intensity tests at 5 different temperatures (25, 40, 55, 70, and 85 °C) and 12 different illumination intensities from 10% to 120% of the AM1.5 irradiation in 10% steps. For each of the 60 combinations, an  $I-V$  measurement was performed, covering a broad

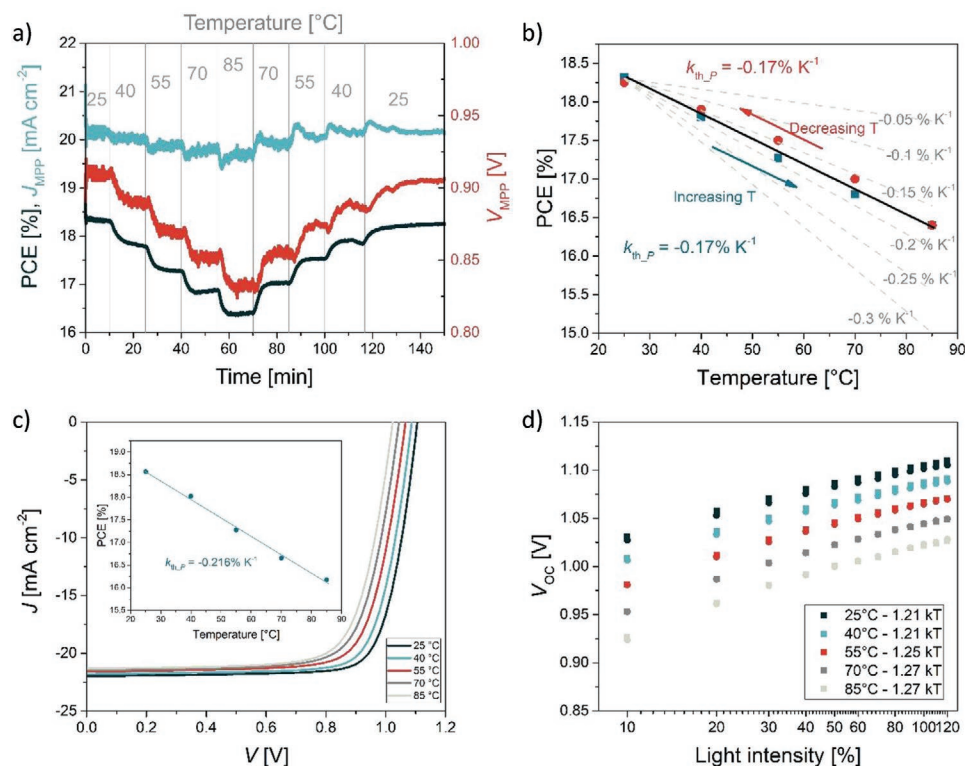


**Figure 4.** a) MPP track of the fabricated perovskite single-junction device with changing the temperature between 25 and 85 °C with a 15 °C step.  $J_{MPP}$  (blue) and  $V_{MPP}$  (red) are also plotted. b) PCE in dependence on temperature. PCE points for each temperature were taken from the MPP track just before the temperature change. PCE for both increasing (blue) and decreasing (red) temperature direction are shown. The linear fit shows the temperature coefficients: solid line shows the measured one, while dashed lines indicate how other  $k_{th,P}$  values would manifest. c)  $J$ - $V$  characteristics at 100  $mW\ cm^{-2}$  intensity. Inset show calculated  $k_{th,P}$  from those measurements. d)  $V_{OC}$  dependence on light intensity and temperature for the tested perovskite device. From the slope, ideality factor is calculated for each of the temperatures.

range of light intensity and temperature combinations. The results are summarized in Figure 4c,d. In Figure 4c  $J$ - $V$  characteristics at different temperatures and 100% illumination intensity are plotted together. Similarly to the MPP test, the main change (drop) is in  $V_{OC}$ ; there is also a slight decrease in  $J_{SC}$ , validating the observed minor  $J_{MPP}$  drop in the MPP test. From the PCE at one-sun, we can again determine the  $k_{th,P}$  the same way as above:  $k_{th,P}$  around  $-0.21\% K^{-1}$  is obtained this way and is shown as an inset in Figure 4c. This value is similar, but also slightly higher than the one derived from MPP tracking. While this adds additional confirmation for our approach and extracted values, it could also indicate that frequent polling, applying external bias other than the  $V_{MPP}$ , light soaking start-stop operation is more demanding for the devices than continuous MPP tracking. This shows that extracting temperature coefficients has to be done with great care to not be influenced by potential device degradation or light-soaking effects. We speculate that this can be one of the reasons for the variation in the reported results.

Furthermore, we compare  $V_{OC}$  at different temperatures and light intensities in the tested range. For all the 5 temperatures tested, a logarithmic dependence of  $V_{OC}$  versus light intensity is apparent, from which the ideality factor  $n$  can be calculated ( $n = \text{slope}/kT$ ). The absolute ideality factor varies slightly from batch-to-batch but is constant at around  $\approx 1.27$  for all the temperatures. The voltage temperature coefficient

$\beta = k_{th,Voc} = -0.12\% K^{-1}$  as shown in Figure S9 (Supporting Information). Additionally, in Figure S9 (Supporting Information) we show  $J_{SC}$ , FF, and PCE dependence for the tested set of temperatures and light intensities. Under one sun the  $J_{SC}$  drop for the  $\Delta T = 60\ K$  is around  $0.7\ mA\ cm^{-2}$ , which yields a current temperature coefficient  $\alpha = k_{th,Jsc} = -0.054\% K^{-1}$ . This is slightly higher than observed for  $J_{MPP}$  in the MPP track and as mentioned above indicates that at MPP the devices are slightly more stable than when performing  $I$ - $V$  measurements as also confirmed by a slightly lower  $k_{th,P}$ . Potentially, the FF drop is lower in the MPP track than in the  $I$ - $V$  measurement, where a drop of 5% over  $\Delta T = 60\ K$  is measured (Figure S9, Supporting Information). The FF is also higher at lower light intensities, pointing out that even our small area devices have potential series resistance losses in the contacts. In Figure S9 (Supporting Information), a PCE is normalized to the PCE at 25 °C and shown in dependence of light intensity in linear scale. For the lower intensity at the elevated temperature, the relative drop in PCE is higher. However, it is unlikely that the device would often operate at a higher temperature and lower intensity since the high intensity is a source of higher temperature (unless a sudden cloud appears on a sunny hot day).

Finally, to see the effect of temperature on  $J_{SC}$  in more detail, we performed temperature-dependent EQE measurements. The results are shown in Figure S10 (Supporting Information).

Due to experimental limitations, temperatures only up to 41 °C could be reached. Nevertheless, a clear trend is visible near the bandgap wavelength, showing a bandgap increase with temperature, which has also been reported in the literature.<sup>[62,63]</sup> Otherwise, the spectra are largely unchanged. The drop between 25 and 41 °C is 0.2 mA cm<sup>-2</sup>. This fits well with the 0.16 mA cm<sup>-2</sup> change of  $J_{SC}$  in the same temperature range.

## 2.4. Energy Yield

Integrating the above-measured temperature data into our previously developed optical energy yield algorithm,<sup>[48]</sup> we can now track the predicted output of the rooftop tested devices. Using optical simulations based on combined ray-tracing/transfer matrix method,<sup>[64]</sup> we obtain absorption spectra of the device stack under different incident angles as well as under diffuse light irradiance that are needed to include the sun path and type of solar irradiance. We consider the perovskite single-junction device with the layer stack as used in the experiment and described above. In the optical simulations, we also include the glass cover from our measurement box, which induces roughly 8% additional reflection losses. The  $n$  and  $k$  values were determined via ellipsometry and  $R$  and  $T$  method and are the same as in our previous research.<sup>[48]</sup> Excluding the box glass cover, the superstrate configuration of perovskite single-junction solar cells already resembles module integration; only a thicker glass with little additional parasitic absorption and back side lamination, not affecting the optics, would have to be utilized. As the optics of the cell is only affected by the sun position and device structure, and not other weather conditions, optical part of our results can be translated to any location.

The direct and diffuse solar irradiance contributions<sup>[65]</sup> were measured with pyranometers on the rooftop and averaged over 1 h for simulations. The spectral changes were measured with a spectrometer. Reflected irradiance  $G$  albedo was then calculated from  $G_{inc}$ , we assume a spectrally independent factor of 0.2, which describes well the ground reflection characteristics of our rooftop. Thus, we consider these three contributions to the current: direct, diffuse and reflected albedo; all three are depicted in Figure S11 (Supporting Information). Due to a very low amount of albedo reflected light, we believe that other reflectivity or spectral dependence would not change the result. The final, total  $J_{SC}$  is a sum of these three contributions ( $J_{SC_{total}} = J_{SC_{direct}} + J_{SC_{diffuse}} + J_{SC_{albedo}}$ ). The  $V_{OC}$  and FF dependency on light intensity are obtained from the laboratory measurements at different temperatures and light intensities, as explained above. To obtain a denser dataset and improve accuracy, the  $V_{OC}$  and FF data between measurement values were interpolated.

The power generated by the cell at any moment can be expressed as

$$P(t, T_{cell}) = J_{SC_{total}}(t, T_{cell}, Irr\_spectrum) \cdot V_{OC}(T_{cell}, G_{inc}) \cdot FF(T_{cell}, G_{inc}) \quad (2)$$

Where the  $Irr\_spectrum$  is the spectrally resolved solar irradiance  $G_{inc}$ . Alternatively, also a simplified version can be used. There, instead of individual  $V_{OC}$  and FF values at different

cell temperatures, only  $V_{OC}$  and FF at different light intensities at 25 °C and the temperature coefficient  $k_{th\_P}$  can be used. First, the power  $P_0$  without temperature deviation from 25 °C is calculated and then weighted with  $k_{th\_P}$  depending on the  $T_{cell}$

$$P_0 = J_{SC_{total}} \cdot V_{OC} \cdot FF \quad (3)$$

$$P = P_0 \left( 1 + k_{th\_P} \cdot (T_{cell} - 25 \text{ } ^\circ\text{C}) \right) \quad (4)$$

In Figure 5a, the MPP track data obtained from our rooftop test site and the calculated energy are compared, with 3 selected days with different stages of degradation shown in more detail in Figure S11 (Supporting Information). We consider two calculated cases as presented by Equation (2) or Equations (3) and (4). Despite the greater complexity of the model described by Equation (2), there is very little, almost negligible difference between the two calculation procedures. Compared to the measurement, our calculated power outputs with both procedures match very well, and we get an excellent match for the first few days of solar cell operation. Interestingly, we do not observe a significant reversible degradation as the generated power in both morning and evening hours match the predicted one well, which could be connected to the p–i–n architecture of our devices.

However, over time the difference between simulated and measured energy output is increasing. These changes with time can be attributed to the slow degradation of the cell under test. Thus, using the temperature-dependent energy yield modelling procedure we can not only predict the expected energy output, but also track and evaluate the degradation of our devices from comparison between measured and predicted energy output. Figure 5b shows the performance ratio of several devices tested on the rooftop, calculated as the ratio between measured and simulated (predicted) energy in percentage. The data obtained from MPP measurements are shown with symbols and thick lines were added as guides to the eye. Depending on the device, different speed of degradation can be observed despite initially similar PCE = ~18.5%. For the best cell, the  $T_{50}$ , time in our case when the power output drops below 50% of the expected one, was around 35 days. There are several possible reasons for different and fast degradation. The most likely one is successfulness of encapsulation in combination with rainy weather (e.g., moisture ingress into the device, see Figures S3 and S4 (Supporting Information) for photographs of devices after testing) or that long-term stability of the devices could be connected with defects that are not visible when measuring under STC. As shown in Figure S6 (Supporting Information) the degradation severely, and mostly, affects FF. Consequently, while the developed temperature-dependent energy yield model itself is not able to point to the parameter that is affected the most (for this  $I$ – $V$  measurements are necessary), its complexity is nevertheless needed as simple estimations for degradation, e.g.,  $J_{MPP}(G_{inc}, T_{air})$ , are not sufficient. It is also worth noting that devices 6 and 7 that were mounted in late October degrade much slower in the initial phase of outdoor testing than previous devices. Whether this is due to batch-to-batch variations or the colder and less sunny weather affects devices less, remains unclear.

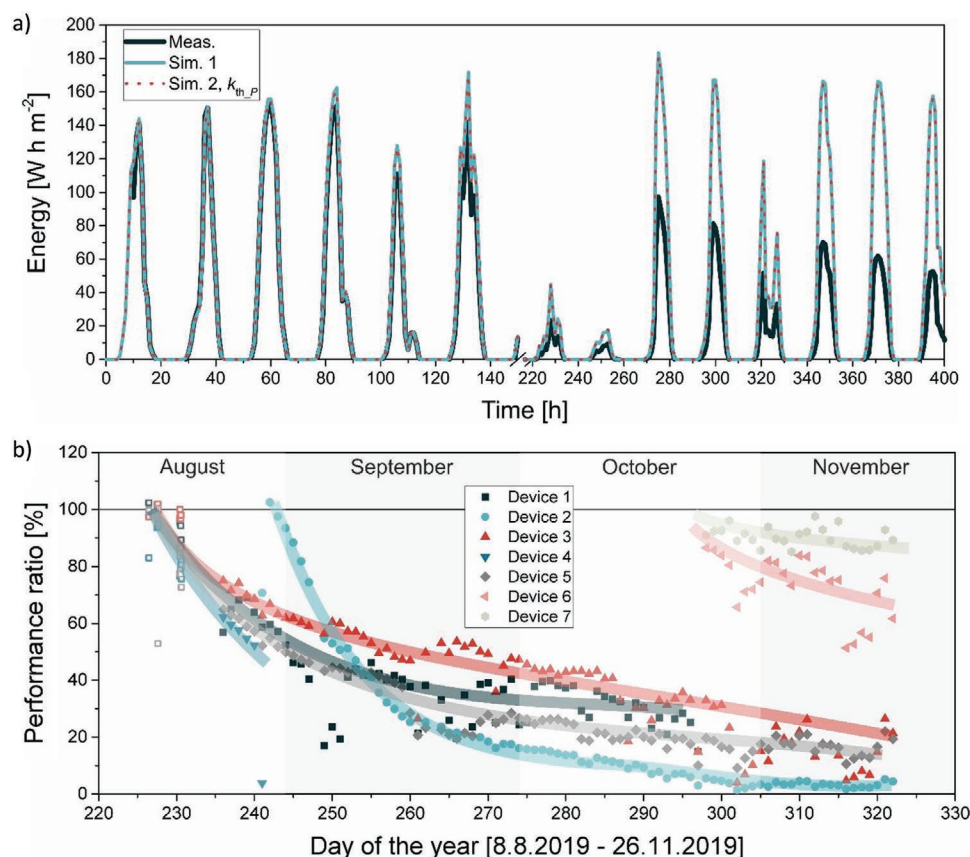


**Figure 5.** a) Comparison between measured (black) and simulated energy of the outdoor tested solar cell. A zoom-in of the three selected days showing more details is presented in Figure S11 (Supporting Information). In the first case (blue), we assumed the values obtained from  $J$ - $V$  characteristics at different temperatures and light intensities. In the second (red), a  $k_{th,p} = -0.17\% K^{-1}$  obtained from MPP tracking at 100% AM1.5G and different temperatures were used. Over time the difference between measurements and simulations increase, thus in b) degradation analysis from the simulated energy yield is shown for 7 different devices that were mounted at different times. The symbols show calculated performance ratio from measurements, while the thick lines were added to guide the eye. The tests lasted from 15.8.2019 to the 18.11.2019. In the first few days, the devices 1, 3, 4, and 5 were MPP tracked, but the data were not recorded. Their energy yield could still be estimated from the  $I$ - $V$  measurements performed at that time (marked with open symbols).

Disentangling different degradation mechanisms will be a part of future investigations.

Finally, using our energy yield model, we can now compare different locations and climate conditions if spectral and temperature data are available. We chose three locations in the USA: Phoenix, Washington D.C and Golden, with different temperatures and irradiation per year. Data for a typical meteorological year is obtained from NREL,<sup>[66]</sup> the locations and averaged irradiance spectra are shown in Figure S12 (Supporting Information). As expected, the energy output is the highest where solar irradiation is the highest (Phoenix). Interestingly, due to low  $k_{th,p}$  of perovskite solar cells, the temperature performance penalty is very low: almost negligible, less than 1% relative for Golden with an average  $T_{cell} = 20$  °C in operation. Even in Phoenix, the hottest out of the three locations with the average operational solar cell temperature of 44 °C, the temperature penalty is less than 5%. Owing to their very low temperature coefficient, the perovskite solar cells have a very stable power output, even in the hottest weather conditions (Figure 6).

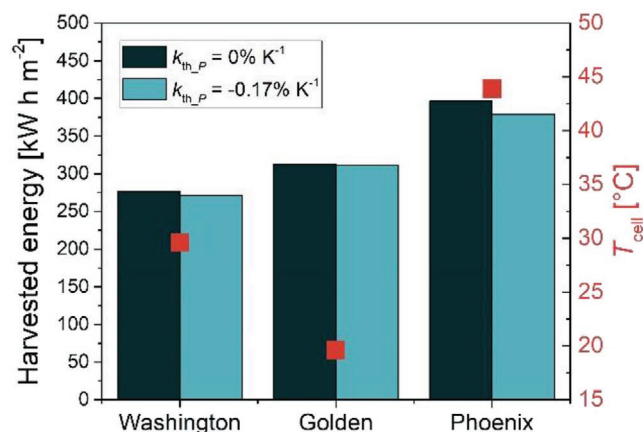


**Figure 6.** Energy yield analysis for three locations in the USA for a typical meteorological year (TMY). The same solar cell as used in the modeling above was assumed. On the right axis, the average  $T_{cell}$  during operation is plotted.



### 3. Conclusion

We showed one of the first outdoor field tests of perovskite single-junction devices. The fabricated solar cells with the active area  $>1 \text{ cm}^2$  and average PCE of 18.5% were placed on the rooftop and tested by MPP tracking and periodic  $I$ - $V$  measurements, while the weather conditions were monitored. We analyzed solar cell performance in relation to the incident solar irradiance and air temperature. From the data, we calculated the nominal operating cell temperature (NOCT) to be  $43 \text{ }^\circ\text{C}$  and also observed a weak effect of solar irradiance  $G_{\text{inc}}$  on voltage. To confirm this, we performed extensive laboratory tests under controlled conditions, investigating perovskite solar cell performance under different light intensities (10% to 120% of AM1.5) and temperatures (from 25 to  $85 \text{ }^\circ\text{C}$ ). The devices showed excellent stability up to  $85 \text{ }^\circ\text{C}$ . From the MPP tracking and  $I$ - $V$  measurements, we obtained a low temperature coefficient  $k_{\text{th},P} = 0.17\% \text{ K}^{-1}$  in the temperature range between 25 and  $85 \text{ }^\circ\text{C}$ . The drop in performance under elevated temperatures is strongly connected to the drop in  $V_{\text{OC}}$  with  $k_{\text{th},V_{\text{OC}}} = -0.12\% \text{ K}^{-1}$ , which, however, is much lower than  $k_{\text{th},V_{\text{OC}}}$  of the established PV technologies. These results show that perovskite solar cells are highly suitable for operation under elevated temperatures.

By combining our findings in the laboratory measurements and weather data with our optical model, we develop a temperature-dependent energy yield model. In the beginning of the field test, the measured and simulated values match well, validating the model. With the increasing time of testing, the difference gradually increases, indicating the degradation of our devices. The developed temperature-dependent energy yield model can therefore be used to predict the energy output of perovskite solar cells in field testing on a chosen location or analyze possible degradation if the dynamic MPP tracking data are available.

### 4. Experimental Section

**Perovskite Materials:** Anhydrous DMSO (dimethyl sulfoxide), DMF (dimethylformamide), and ethanol were purchased from Sigma Aldrich.  $\text{C}_{60}$  (purity = 99.9%) was purchased from Sigma Aldrich. FAI (formamidinium iodide) and MABr (methylammonium bromide) were purchased from Dyanamo.  $\text{PbI}_2$  and  $\text{PbBr}_2$  were bought from TCI. CsI was purchased from abcr GmbH. MeO-2PACz was synthesized as described in the previous publication.<sup>1571</sup>

**Perovskite Solar Cell Preparation:** The fabricated perovskite sub cell has an inverted (p-i-n) planar structure and a layer configuration of glass/ITO/MeO-2PACz/Perovskite/ $\text{C}_{60}/\text{SnO}_2/\text{Cu}$ . All the spin-coating layer deposition steps were conducted in a nitrogen atmosphere. The hole transport material MeO-2PACz ( $1.3 \text{ mg mL}^{-1}$  in ethanol) was deposited using spin-coating (3000 rpm for 30 s) and annealed for 10 min at  $100 \text{ }^\circ\text{C}$ . The perovskite was prepared following the typical “triple cation” process as it was previously described.<sup>1481</sup> 100  $\mu\text{L}$  of perovskite solution was then spread on the substrate and spun using one step spin-coating process (4000 rpm for 35 s). 25 s after the start of a spinning, films were washed with 400  $\mu\text{L}$  ethyl acetate anti-solvent drop. The films were annealed at  $100 \text{ }^\circ\text{C}$  for 1 h. Afterward, 23 nm  $\text{C}_{60}$  was thermally evaporated at a rate of  $0.15 \text{ A s}^{-1}$  at  $390 \text{ }^\circ\text{C}$ . 20 nm  $\text{SnO}_2$  were prepared by thermal ALD in an Arradiance GEMStar reactor. Tetrakis(dimethylamino)tin(IV) (TDMASn) was used as the Sn precursor and water was used as oxidant. Finally, a 100 nm thick Cu back electrode was evaporated as a top contact. A two-component resin from R&G Faserverbundwerkstoffe GmbH was used for encapsulation. The resin was put on the substrate edge, then the substrate was covered with a glass.

**Optical Simulations:** The optical simulations were done using CROWM<sup>164,167</sup>. The simulator is based on combined ray and wave optics models. As the input parameters, realistic thicknesses and experimentally determined refractive indices of the materials were employed. The imaginary part of the refractive index of the perovskite absorber was wavelength-shifted to obtain the different bandgaps. The main outputs of the simulator are total reflectance, transmittance and absorptance in each layer. Their solar-spectrum wavelength integration equals to the generated  $J_{\text{SC}}$  or the equivalent  $J_{\text{SC}}$  loss in each individual layer. The simulations were carried out in the wavelength range from 350 to 800 nm, which is a sufficiently broad range for the analyzed perovskite single-junction solar cells.

**Device Characterization:** The current-voltage ( $I$ - $V$ ) measurements were performed under standard test conditions ( $25 \text{ }^\circ\text{C}$ , LED sun simulator, Wavelabs, class AAA), adjusted with a calibrated KG3 silicon reference cell (Fraunhofer ISE). The scan rate was  $0.250 \text{ V s}^{-1}$  with a voltage step of 20 mV. The light intensity dependent  $I$ - $V$  measurements were performed by adjusting the LEDs of the sun simulator. The light intensity was then swept from 10% AM1.5 to 120% AM1.5 in 10% steps. The temperature was set using thermal chuck. The EQE was measured as a function of wavelength from 300 to 850 nm with a step of 10 nm using an Oriol Instrument's QEPVSI-b system with 300 W xenon arc lamp, controlled by TracQ-Basic software.

**Outdoor Data:** Rooftop MPP tracking and  $I$ - $V$  measurements were performed using an in-house developed  $\mu\text{MPP}$  tracker (<http://lpvo.fe.uni-lj.si/en/services/pv-monitoring/cell-monitoring/>). Spectrum was measured with spectroradiometer EKO MS-711, global and diffuse irradiance were measured with Kipp&Zonen CMP21 pyranometers. Temperature was detected using a digital temperature sensor attached to the back-side of the device.

### Supporting Information

Supporting Information is available from the Wiley Online Library or from the author.

### Acknowledgements

The authors thank Holger Rhein for patterning the ITO substrates, and Eike Köhnen, Lukas Kegelmann and Lars Korte for fruitful discussions. The authors acknowledge the funding by the German Federal Ministry of Education and Research (BMBF) via program “Materialforschung fuer die Energiewende” (Grant No. 03SF0540), bilateral project BI-DE/2017-2019/004 (German Academic Exchange Service (DAAD)), and Slovene Research Agency (ARRS) and research programs P2-0197 and J2-1727. The authors thank the Helmholtz association for funding the project TAPAS within the EU partnering program. A.M. acknowledges funding by the Research Council of Lithuania under grant agreement no. S-MIP-19-5/SV3-1079 of the SAM project. The research leading to these results has partly received funding from the European Union's Horizon 2020 research and innovation program under grant agreement no. 763977 of the PerTPV project.

### Conflict of Interest

The authors declare no conflict of interest.

### Keywords

energy yields, field tests, outdoor measurements, perovskite solar cells, temperature coefficients

Received: February 4, 2020  
Revised: May 10, 2020  
Published online:

- [1] "Best Research-Cell Efficiency Chart | Photovoltaic Research | NREL," <https://www.nrel.gov/pv/cell-efficiency.html> (accessed: April, 2019).
- [2] Y. Zhou, Y. Zhao, *Energy Environ. Sci.* **2019**, *12*, 1495.
- [3] K. Domanski, J.-P. Correa-Baena, N. Mine, M. K. Nazeeruddin, A. Abate, M. Saliba, W. Tress, A. Hagfeldt, M. Grätzel, *ACS Nano* **2016**, *10*, 6306.
- [4] Z. Ahmad, M. A. Najeeb, R. A. Shakoor, A. Alashraf, S. A. Al-Muhtaseb, A. Soliman, M. K. Nazeeruddin, *Sci. Rep.* **2017**, *7*, 15406.
- [5] C. C. Boyd, R. Cheacharoen, K. A. Bush, R. Prasanna, T. Leijtens, M. D. McGehee, *ACS Energy Lett.* **2018**, *3*, 1772.
- [6] T. Leijtens, K. Bush, R. Cheacharoen, R. Beal, A. Bowring, M. D. McGehee, *J. Mater. Chem. A* **2017**, *5*, 11483.
- [7] R. Wang, M. Mujahid, Y. Duan, Z.-K. Wang, J. Xue, Y. Yang, *Adv. Funct. Mater.* **2019**, *29*, 1808843.
- [8] K. Domanski, E. A. Alharbi, A. Hagfeldt, M. Grätzel, W. Tress, *Nat. Energy* **2018**, *3*, 61.
- [9] J. P. Bastos, U. W. Paetzold, R. Gehlhaar, W. Qiu, D. Cheyns, S. Surana, V. Spampinato, T. Aernouts, J. Poortmans, *Adv. Energy Mater.* **2018**, *8*, 1800554.
- [10] T. Sekimoto, T. Matsui, T. Nishihara, R. Uchida, T. Sekiguchi, T. Negami, *ACS Appl. Energy Mater.* **2019**, *2*, 5039.
- [11] T. Abzieher, S. Moghadamzadeh, F. Schackmar, H. Eggers, F. Sutterlüti, A. Farooq, K. Habicht, R. Schmager, A. Mertens, R. Azmi, L. Klotz, J. A. Schwenzler, M. Hetterich, U. Lemmer, B. S. Richards, M. Powalla, U. W. Paetzold, *Adv. Energy Mater.* **2019**, *9*, 1802995.
- [12] S. Seo, S. Jeong, C. Bae, N.-G. Park, H. Shin, *Adv. Mater.* **2018**, *30*, 1801010.
- [13] R. Cheacharoen, N. Rolston, D. Harwood, K. A. Bush, R. H. Dauskardt, M. D. McGehee, *Energy Environ. Sci.* **2018**, *11*, 144.
- [14] T. Matsui, T. Yamamoto, T. Nishihara, R. Morisawa, T. Yokoyama, T. Sekiguchi, T. Negami, *Adv. Mater.* **2019**, *31*, 1806823.
- [15] L. Kegelmann, P. Tockhorn, C. M. Wolff, J. A. Márquez, S. Caicedo-Dávila, L. Korte, T. Unold, W. Lövenich, D. Neher, B. Rech, S. Albrecht, *ACS Appl. Mater. Interfaces* **2019**, *11*, 9172.
- [16] Y. Zhou, X. Yin, Q. Luo, X. Zhao, D. Zhou, J. Han, F. Hao, M. Tai, J. Li, P. Liu, K. Jiang, H. Lin, *ACS Appl. Mater. Interfaces* **2018**, *10*, 31384.
- [17] Q. Jiang, Y. Zhao, X. Zhang, X. Yang, Y. Chen, Z. Chu, Q. Ye, X. Li, Z. Yin, J. You, *Nat. Photonics* **2019**, *13*, 460.
- [18] S. Bai, P. Da, C. Li, Z. Wang, Z. Yuan, F. Fu, M. Kawecki, X. Liu, N. Sakai, J. T.-W. Wang, S. Huettner, S. Buecheler, M. Fahlman, F. Gao, H. J. Snaith, *Nature* **2019**, *571*, 245.
- [19] X. Li, X. Li, M. Tschumi, H. Han, S. Babkair, R. A. Alzubaydi, A. A. Ansari, S. S. Habib, M. K. Nazeeruddin, S. M. Zakeeruddin, M. Grätzel, *Energy Technol.* **2015**, *3*, 551.
- [20] Y. Reyna, M. Salado, S. Kazim, A. Pérez-Tomas, S. Ahmad, M. Lira-Cantu, *Nano Energy* **2016**, *30*, 570.
- [21] V. Stoichkov, N. Bristow, J. Troughton, F. De Rossi, T. M. Watson, J. Kettle, *Sol. Energy* **2018**, *170*, 549.
- [22] F. Bella, G. Griffini, J.-P. Correa-Baena, G. Saracco, M. Grätzel, A. Hagfeldt, S. Turri, C. Gerbaldi, *Science* **2016**, *354*, 203.
- [23] M. V. Khenkin, K. M. Anoop, I. Visoly-Fisher, Y. Galagan, F. Di Giacomo, B. R. Patil, G. Sherafatipour, V. Turkovic, H.-G. Rubahn, M. Madsen, T. Merckx, G. Uytterhoeven, J. P. A. Bastos, T. Aernouts, F. Brunetti, M. Lira-Cantu, E. A. Katz, *Energy Environ. Sci.* **2018**, *11*, 739.
- [24] J. P. Bastos, G. Uytterhoeven, W. Qiu, U. W. Paetzold, D. Cheyns, S. Surana, J. Rivas, M. Jaysankar, W. Song, T. Aernouts, J. Poortmans, R. Gehlhaar, *ACS Appl. Mater. Interfaces* **2019**, *11*, 16517.
- [25] B. Chen, J. Song, X. Dai, Y. Liu, P. N. Rudd, X. Hong, J. Huang, *Adv. Mater.* **2019**, *31*, 1902413.
- [26] J. A. Schwenzler, L. Rakocevic, R. Gehlhaar, T. Abzieher, S. Gharibzadeh, S. Moghadamzadeh, A. Quintilla, B. S. Richards, U. Lemmer, U. W. Paetzold, *ACS Appl. Mater. Interfaces* **2018**, *10*, 16390.
- [27] P. Holzhey, M. Saliba, *J. Mater. Chem. A* **2018**, *6*, 21794.
- [28] M. V. Khenkin, E. A. Katz, A. Abate, G. Bardizza, J. J. Berry, C. Brabec, F. Brunetti, V. Bulovic, Q. Burlingame, A. Di Carlo, R. Cheacharoen, Y.-B. Cheng, A. Colmann, S. Cros, K. Domanski, M. Duszka, C. J. Fell, S. R. Forrest, Y. Galagan, D. Di Girolamo, M. Grätzel, A. Hagfeldt, E. von Hauff, H. Hoppe, J. Kettle, H. Köbler, M. S. Leite, S. F. Liu, Y.-L. Loo, J. M. Luther, C.-Q. Ma, M. Madsen, M. Manceau, M. Matheron, M. McGehee, R. Meitzner, M. K. Nazeeruddin, A. F. Nogueira, Ç. Odabasi, A. Osherov, N.-G. Park, M. O. Reese, F. De Rossi, M. Saliba, U. S. Schubert, H. J. Snaith, S. D. Stranks, W. Tress, P. A. Troshin, V. Turkovic, S. Veenstra, I. Visoly-Fisher, A. Walsh, T. Watson, H. Xie, R. Yildirim, S. M. Zakeeruddin, K. Zhu, M. Lira-Cantu, *Nat. Energy* **2020**, *5*, 35.
- [29] Y. Yuan, J. Huang, *Acc. Chem. Res.* **2016**, *49*, 286.
- [30] A. Extnance, *Nature* **2019**, *570*, 429.
- [31] W. Song, T. Aernouts, *J. Phys. Energy* **2020**, *2*, 021003.
- [32] K. Domanski, B. Roose, T. Matsui, M. Saliba, S.-H. Turren-Cruz, J.-P. Correa-Baena, C. R. Carmona, G. Richardson, J. M. Foster, F. De Angelis, J. M. Ball, A. Petrozza, N. Mine, M. K. Nazeeruddin, W. Tress, M. Grätzel, U. Steiner, A. Hagfeldt, A. Abate, *Energy Environ. Sci.* **2017**, *10*, 604.
- [33] L. Jiang, J. Lu, S. R. Raga, J. Sun, X. Lin, W. Huang, F. Huang, U. Bach, Y. B. Cheng, *Nano Energy* **2019**, *58*, 687.
- [34] W. Tress, K. Domanski, B. Carlsen, A. Agarwalla, E. A. Alharbi, M. Graetzel, A. Hagfeldt, *Nat. Energy* **2019**, *4*, 568.
- [35] W. Shockley, H. J. Queisser, *J. Appl. Phys.* **1961**, *32*, 510.
- [36] O. Dupré, R. Vaillon, M. A. Green, *Sol. Energy Mater. Sol. Cells* **2015**, *140*, 92.
- [37] G. Friesen, D. Pavanello, A. Virtuani, in *Proc. 5th World Conf. on Photovoltaic Energy Conversion*, **2010**, pp. 4248–4252.
- [38] M. Kasu, J. Abdu, S. Hara, S. Choi, Y. Chiba, A. Masuda, *Jpn. J. Appl. Phys.* **2018**, *57*, 08RG18.
- [39] J. Haschke, J. P. Seif, Y. Riesen, A. Tomasi, J. Cattin, L. Tous, P. Choulat, M. Aleman, E. Cornagliotti, A. Uruena, R. Russell, F. Duerinckx, J. Champlaud, J. Levrat, A. A. Abdallah, B. Aïssa, N. Tabet, N. Wyrsh, M. Despeisse, J. Szlufcik, S. De Wolf, C. Ballif, *Energy Environ. Sci.* **2017**, *10*, 1196.
- [40] S. N. Habisreutinger, T. Leijtens, G. E. Eperon, S. D. Stranks, R. J. Nicholas, H. J. Snaith, *Nano Lett.* **2014**, *14*, 5561.
- [41] L. Cojocar, S. Uchida, Y. Sanehira, V. G. Pedro, J. Bisquert, J. Nakazaki, T. Kubo, H. Segawa, *Chem. Lett.* **2015**, *44*, 1557.
- [42] T. J. Jacobsson, W. Tress, J.-P. Correa-Baena, T. Edvinsson, A. Hagfeldt, *J. Phys. Chem. C* **2016**, *120*, 11382.
- [43] F. Fu, T. Feurer, T. P. Weiss, S. Pisoni, E. Avancini, C. Andres, S. Buecheler, A. N. Tiwari, *Nat. Energy* **2017**, *2*, 16190.
- [44] Y. Deng, C. H. V. Brackley, X. Dai, J. Zhao, B. Chen, J. Huang, *Sci. Adv.* **2019**, *5*, eaax7537.
- [45] A. K. Jena, Y. Numata, M. Ikegami, T. Miyasaka, *J. Mater. Chem. A* **2018**, *6*, 2219.
- [46] R. Gehlhaar, T. Merckx, W. Qiu, T. Aernouts, *Global Challenges* **2018**, *2*, 1800008.
- [47] M. T. Hörantner, H. J. Snaith, *Energy Environ. Sci.* **2017**, *10*, 1983.
- [48] M. Jošt, E. Köhnen, A. B. Morales-Vilches, B. Lipovšek, K. Jäger, B. Maccò, A. Al-Ashouri, J. Krc, L. Korte, B. Rech, R. Schlattmann, M. Topic, B. Stannowski, S. Albrecht, *Energy Environ. Sci.* **2018**, *11*, 3511.
- [49] J. Lehr, M. Langenhorst, R. Schmager, S. Kirner, U. Lemmer, B. S. Richards, C. Case, U. W. Paetzold, *Sustainable Energy Fuels* **2018**, *2*, 2754.
- [50] R. Schmager, M. Langenhorst, J. Lehr, U. Lemmer, B. S. Richards, U. W. Paetzold, *Opt. Express* **2019**, *27*, A507.

- [51] E. Köhnen, M. Jošt, A. B. Morales-Vilches, P. Tockhorn, A. Al-Ashouri, B. Macco, L. Kegelmann, L. Korte, B. Rech, R. Schlatmann, B. Stannowski, S. Albrecht, *Sustainable Energy Fuels* **2019**, *3*, 1995.
- [52] O. Dupré, B. Niesen, S. De Wolf, C. Ballif, *J. Phys. Chem. Lett.* **2018**, *9*, 446.
- [53] "IEC 61853-1:2011 | IEC Webstore | rural electrification, solar power, LVDC," <https://webstore.iec.ch/publication/6035> (accessed: December, 2019).
- [54] T. Malinauskas, D. Tomkute-Luksiene, R. Sens, M. Daskeviciene, R. Send, H. Wonneberger, V. Jankauskas, I. Bruder, V. Getautis, *ACS Appl. Mater. Interfaces* **2015**, *7*, 11107.
- [55] E. Kasparavicius, A. Magomedov, T. Malinauskas, V. Getautis, *Chem. - Eur. J.* **2018**, *24*, 9910.
- [56] M. Saliba, T. Matsui, J.-Y. Seo, K. Domanski, J.-P. Correa-Baena, M. K. Nazeeruddin, S. M. Zakeeruddin, W. Tress, A. Abate, A. Hagfeldt, M. Grätzel, *Energy Environ. Sci.* **2016**, *9*, 1989.
- [57] A. Al-Ashouri, A. Magomedov, M. Roß, M. Jošt, M. Talaikis, G. Chistiakova, T. Bertram, J. A. Márquez, E. Köhnen, E. Kasparavicius, S. Levenco, L. Gil-Escrig, C. J. Hages, R. Schlatmann, B. Rech, T. Malinauskas, T. Unold, C. A. Kaufmann, L. Korte, G. Niaura, V. Getautis, S. Albrecht, *Energy Environ. Sci.* **2019**, *12*, 3356.
- [58] J. A. Raiford, C. C. Boyd, A. F. Palmstrom, E. J. Wolf, B. A. Fearon, J. J. Berry, M. D. McGehee, S. F. Bent, *Adv. Energy Mater.* **2019**, *9*, 1902353.
- [59] J. W. Stultz, *J. Energy* **1979**, *3*, 363.
- [60] SunPower, "X-Series Solar Panels," *SunPower-United States* <https://us.sunpower.com/solar-panels-technology/x-series-solar-panels> (accessed: January, 2020).
- [61] "BISOL Premium series (monocrystalline)," <http://www.bisol.com/en/products/pv-modules/bisol-premium-series-mono.html> (accessed: August, 2019).
- [62] K. Wu, A. Bera, C. Ma, Y. Du, Y. Yang, L. Lib, T. Wu, *Phys. Chem. Chem. Phys.* **2014**, *16*, 22476.
- [63] R. L. Milot, G. E. Eperon, H. J. Snaith, M. B. Johnston, L. M. Herz, *Adv. Funct. Mater.* **2015**, *25*, 6218.
- [64] B. Lipovšek, A. Campa, F. Guo, C. J. Brabec, K. Forberich, J. Krc, M. Topic, *Opt. Express* **2017**, *25*, A176.
- [65] B. Kirn, K. Brecl, M. Topic, *Sol. Energy* **2015**, *113*, 212.
- [66] "NSRDB Viewer | National Solar Radiation Database (NSRDB)," <https://nslrdb.nrel.gov/nslrdb-viewer> (accessed: July, 2018).
- [67] B. Lipovšek, J. Krč, M. Topič, *IEEE J. Photovoltaics* **2018**, *8*, 783.